

Unveiling the cosmological information beyond linear scales: forecasts for sufficient statistics

M. Wolk^{*}, J. Carron and I. Szapudi

Institute for Astronomy, University of Hawaii, 2680 Woodlawn Drive, Honolulu, HI, 96822

14 June 2022

ABSTRACT

Beyond the linear regime, Fourier modes of cosmological random fields become correlated, and the power spectrum of density fluctuations contains only a fraction of the available cosmological information. To unveil this formerly hidden information, the A^* non-linear transform was introduced; it is optimized both for the nonlinearities induced by gravity and observational noise. Quantifying the resulting increase of our knowledge of cosmological parameters, we forecast the constraints from the angular power spectrum and that of A^* from $\ell \sim 200$ to 3000 for upcoming galaxy surveys such as: the Wide-Field Infrared Survey Telescope (WFIRST), the Large Synoptic Survey Telescope (LSST), Euclid, the Hyper Suprime-Cam (HSC) and the Dark Energy Survey (DES). We find that at low redshifts this new data analysis strategy can double the extracted information, effectively doubling the survey area. To test the accuracy of our forecasting and the power of our data analysis methods, we apply the A^* transformation to the latest release of the Canada-France-Hawaii-Telescope Legacy Survey (CFHTLS) Wide. While this data set is too sparse to allow for more than modest gains ($\sim 1.1 - 1.2$), the realized gain from our method is in excellent agreement with our forecast, thus verifying the robustness of our analysis and prediction pipelines.

Key words: methods: cosmology: large-scale-structure of the Universe

1 INTRODUCTION

Within the successful inflationary paradigm of cosmology, the small initial density fluctuations obey Gaussian statistics. This fact makes power spectra particularly powerful summary statistics: at early times, the amplitude of each wave number carries independent information, and the variance calculated from all of them contains all available information: the random phases carry no cosmological significance. In this case, an hypothetical ideal observation of the spectrum unlocks an amount of information proportional to the number of resolved Fourier modes. For this reason, the power spectrum is among the most widely used statistic to characterize the large scale structures in the Universe. From it, a wealth of information is to be gained constraining cosmological models as it was successfully shown using large galaxy surveys such as the 2-degree field galaxy survey (e.g., Cole et al. 2005) and the Sloan Digital Sky Survey (e.g., Tegmark et al. 2004). Moreover, the next decades will see the advent of large wide-field surveys that are designed to measure in exquisite detail the two-point statistics of the matter field through weak-lensing or clustering, ultimately targeting fundamental questions such as the nature of dark

energy or neutrino masses.

Unfortunately, there are significant obstacles to clear before the new generation of surveys can achieve their worthwhile goals. In particular, the observational noise and the correlation of Fourier modes developing from non-linear gravitational growth decrease the amount of information accessible to the power spectrum. In the mildly non-linear regime the information saturates at a finite plateau instead of growing sharply with the cube (or square, in the case of projected density) of the maximal resolved wavenumber. At first sight this leads to an impressive mismatch with naive Gaussian expectations (Rimes & Hamilton 2005, 2006; Neyrinck et al. 2006; Neyrinck & Szapudi 2007). It is now well understood that this is mostly due to a finite volume effect (Szapudi & Colombi 1996) built out of two main components: first the “beat coupling” correlating small scales to the survey scale and then the arguably large background mode variance even for large surveys (Rimes & Hamilton 2005, 2006; de Putter et al. 2012; Takada & Hu 2013). In particular, in the case of the noise free dark matter field, inference on traditional cosmological parameters generically suffers substantially from the necessary calibration or reconstruction of the local density (Carron & Szapudi 2014b; Li et al. 2014).

Since all the upcoming cosmological surveys are de-

^{*} E-mail: wolk@ifa.hawaii.edu

manding in resources, it is worth investigating alternative analysis strategies than the power spectrum, with the aim of being more efficient. Mainstream methods include most notably higher-order N -point statistics (e.g., Peebles 1980; Szapudi 2009). The analysis of higher order statistics are however often difficult due to a steep combinatorial complexity, and furthermore gravity drives the matter field towards a regime where they should not be expected to capture information efficiently (Carron & Neyrinck 2012, and references therein). Introduced specifically with efficiency in mind are non-linear transformations, such as the logarithmic mapping (Neyrinck et al. 2009) or variants thereof (Seo et al. 2011; Joachimi & Taylor 2011). While these transforms were originally phenomenologically motivated, Carron & Szapudi (2013) demonstrated how to construct explicitly transforms of the field that capture by design most of the available information, resulting in approximate “sufficient statistics”. Then, Carron & Szapudi (2014a), taking further into account the discreteness effects in galaxy surveys introduced the $A^*(N)$ non-linear transformation as the optimal observable to extract the information content. The latter is the analog of the logarithmic dark matter field δ transform $A = \ln(1 + \delta)$ for galaxy count maps N to which it reduces for large sampling rates.

Non-linear transformations, and more specifically the optimal A^* transformation, take into account discreteness effects and the non-Gaussianity of the field to improve the statistical power of the spectrum. However, it remains somewhat unclear to this day how much overall improvement over standard methods one can expect from this approach. The principal aim of this paper is to estimate the constraining power of the A^* angular power spectrum compared to that of the angular galaxy power spectrum on cosmological parameters in realistic current and future projected surveys.

In order to address this question, we need to capture in a satisfying manner all the effects discussed above. Throughout this work, we adopt a halo occupation distribution model (hereafter HOD, Seljak 2000; Scoccimarro et al. 2001; Kravtsov et al. 2004; Zheng et al. 2005) to describe the galaxy clustering. The cosmic variance is taken into account using the assumption of lognormal field statistics for a $2d$ projected field and the projected galaxy counts are described by multinomial sampling of that field. Carron et al. (2014) have demonstrated that these prescriptions reproduce accurately the statistical properties of the galaxy field.

We proceed as follows. Section 2 presents the modeling that enters our predictions. Described in Section 3 is the fast projected galaxy counts map simulation pipeline that we use, tested on CFHTLS data for accuracy. With this tool we forecast the expected gain in information of the A^* transform for different surveys and parameters, as presented in Section 4. Our predictions are also compared to actual measurements from the CFHTLS data. We summarize and conclude with a discussion in Section 5. Two appendices collect additional technical details of the methodology.

2 MODELING

This section reviews the different ingredients that enter our analysis of the data and forecasts later in section 3. The

statistical aspects of the model are discussed in 2.1. The model takes as necessary input the galaxy two-point correlation function, for which we use the HOD parametrization discussed in 2.2. Finally, our fiducial values for the cosmological and HOD parameters are discussed in 2.3.

2.1 Statistical modeling

Let $\mathbf{N} = (N_1, \dots, N_d)$ be a map of galaxy counts in d cells containing respectively N_1, \dots, N_d objects. We model the map as a discrete sampling of an underlying continuous galaxy field $\rho_g = (\rho_{g,1}, \dots, \rho_{g,d})$. This field is chosen to obey lognormal field statistics, i.e. the map $\mathbf{A} = \ln \rho_g$ is Gaussian. The $d \times d$ covariance matrix of the Gaussian field is related to that of the galaxy field through

$$\omega_{A,ij} = \ln(1 + \omega_{\delta_g,ij}), \quad (1)$$

where ω_{δ_g} is the galaxy two-point function discussed in section 2.2, further filtered as described in the Appendix of Carron et al. (2014) to account for the slight anisotropy induced by the square cells.

To complete the statistical description of the counts, we need discrete sampling of the underlying continuous field. To do so, there at least are two natural choices: Poisson sampling, for which the number of galaxies varies from one map to the other, and multinomial sampling for which the total number of objects is the same in each map. In this study we use the latter. This choice has the main virtue of simplifying the interpretation of the results as there is no need to introduce a Poisson sampling intensity parameter $\langle N \rangle = \bar{N}$, and to marginalize over it in the end. Arguably, one may worry about the difference in cosmic variance and how well it is taken into account compared to a Poisson sampling. As discussed in Appendix B, in practice both sampling methods lead to identical results when performed consistently.

Let f_i be the unmasked fraction of cell i . We set the multinomial sampling probability in cell i to be proportional to that fraction times the galaxy field $\rho_{g,i}$ behind it. Explicitly, the probability for the count map \mathbf{N} in the presence of the galaxy field may be written as

$$P(\mathbf{N}|\rho) = \left(\frac{N_{\text{tot}}!}{N_1! \dots N_d!} \right) \prod_{i=1}^d \left(\frac{f_i \rho_i}{\sum_j f_j \rho_j} \right)^{N_i}, \quad (2)$$

with $N_{\text{tot}} = \sum_i N_i$ is the total number of galaxies in the map.

2.2 Analytical modeling

The key quantity in the above section is the galaxy angular two-point correlation function $\omega(\theta)$. We found that in order to correctly reproduce the behavior of the galaxy field on small scales we need to take into account how galaxies are distributed within the dark matter haloes. To do so, we use the “halo model” (Scoccimarro et al. 2001; Ma & Fry 2000; Peacock & Smith 2000; Cooray & Sheth 2002) which states that the galaxy-galaxy correlation function can be written as a sum of two contributions:

$$\xi(r) = \xi_{1h}(r) + \xi_{2h}(r). \quad (3)$$

The first term, called the one-halo term, comes from pairs of galaxies that reside within the same dark matter halo and

depends on the number of galaxy pairs per halo $\langle N(N-1) \rangle$. The second term, called the two-halo term, is due to pairs of galaxies that reside in two separate dark matter haloes and depends on the number of galaxies per halo $\langle N \rangle$. To calculate the galaxy clustering, we need to describe how galaxies populate dark matter haloes and to do so, we closely follow Zheng et al. (2007) which describes $N(M)$, the number of galaxies in a halo of given mass M , as a sum of two terms: one coming from the central galaxy in the halo $N_c(M)$ and the other coming from the satellites $N_s(M)$. Thus $N(M)$ can be expressed as:

$$N(M) = N_c(M) \times [1 + N_s(M)] \quad (4)$$

where

$$N_c(M) = \frac{1}{2} \left[1 + \operatorname{erf} \left(\frac{\log M - \log M_{\min}}{\sigma_{\log M}} \right) \right], \quad (5)$$

and

$$N_s(M) = \left(\frac{M - M_0}{M_1} \right)^\alpha. \quad (6)$$

Our model has five adjustable parameters: M_{\min} , M_1 , M_0 , α and $\sigma_{\log M}$. For the halo mass function, we use the prescription from Sheth & Tormen (1999). Furthermore, we describe the halo density profile using a Navarro-Frenk-White (NFW) profile (Navarro et al. 1997) and we assume that haloes are biased tracers of the matter distribution using for the halo bias, $b_h(M, z)$, the parametrization from Tinker et al. (2005) calibrated on simulations. More details can be found in Coupon et al. (2012). The knowledge of the cosmology and of the above five HOD parameters allow us to estimate the two-point correlation via Equation 3 and thus its projected counterpart ω .

2.3 Fiducial HOD parameters and cosmology

Our fiducial model for the HOD parameters is based on galaxy observations using the seventh and final version of the Canada-France-Hawaii-Telescope Legacy survey (CFHTLS)¹ and the sample selection of Wolk et al. (2013).

For the purpose of that paper, we restrict our study to the biggest field, W1, which has the highest statistics. The W1 field is approximately a square of $L = 7.46$ degrees on the side, that we divide into 128^2 square cells. Doing so, we can probe the galaxy angular power spectrum in the multipole range $240 \leq k \leq 3100$. We consider four redshift bins: $0.2 < z < 0.4$, $0.4 < z < 0.6$, $0.6 < z < 0.8$ and $0.8 < z < 1.0$. A large bin width ($\Delta_z = 0.2$) ensures a low bin-to-bin contamination.

The cosmological and HOD parameters used in Wolk et al. (2013) are summarized in Tables 1 and 2. These best-fit HOD parameters were derived fitting the angular two-point correlation using the Population Monte Carlo (PMC) technique as implemented in the `CosmoPMC`² package. This fiducial model fixes the A^* -mapping parameters, presented in Table 3 and moreover it means that, by construction, all the CFHTLS simulated maps have the two-point statistics determined by this fiducial model.

Table 1. Cosmological model parameters. The parameters marked with a dagger are kept fixed when analysing the model for the fiducial case.

Ω_m	Ω_K^\dagger	Ω_b^\dagger	w_0	w_a^\dagger	h^\dagger	n_s^\dagger	σ_8
0.27	0.0 [†]	0.045 [†]	-1.0	0.0 [†]	0.70 [†]	0.96 [†]	0.80

Table 3. A^* -mapping parameters for the CFHTLS. \bar{N} is an estimation of the sampling rate and σ_A^2 is the variance of the A field related to the variance of the galaxy field by $\sigma_A^2 = \ln(1 + \sigma_{\delta_g}^2)$.

Redshift bin	σ_A^2	\bar{N}
$0.2 < z < 0.4$	0.274	2.086
$0.4 < z < 0.6$	0.172	5.861
$0.6 < z < 0.8$	0.135	9.684
$0.8 < z < 1.0$	0.120	8.836

2.4 Surveys specificities

As a non-exhaustive but however representative ensemble of upcoming galaxy surveys, we choose to consider configurations close to the ones expected for the Hyper Suprime-Cam³ (HSC), Euclid⁴, the Large Synoptic Survey Telescope⁵ (LSST), the Dark Energy Survey⁶ (DES) and the Wide-Field Infrared Survey Telescope⁷ (WFIRST).

Following Takada & Jain (2009) we model the redshift distribution of the objects through the following one-parameter functional form:

$$\frac{dn(z)}{dz} = n_0 \times 4z^2 \exp\left(-\frac{z}{z_0}\right) \quad (7)$$

where the normalization is fixed to $n_0 \simeq 100 \text{ arcmin}^{-2}$ and z_0 is related to the mean redshift, z_m , by $z_0 = z_m/3$. The only free parameter is z_m and Table 4 shows the values that we pick for each survey. Also shown are the angular number density of galaxies $\bar{n}_g \equiv \int_0^{+\infty} dz dn(z)/dz$. Figure 1 shows the distribution of the number density of objects over the redshift range $z \in [0, 1.0]$. In the case of the CFHTLS-W1 field, we use directly the measured redshift distribution. We build our samples by splitting these distributions into the four different redshift bins $0.2 < z < 0.4$, $0.4 < z < 0.6$, $0.6 < z < 0.8$ and $0.8 < z < 1.0$ for which we have derived the HOD parameters from the CFHTLS.

Since we are interested in the non-linear scales, in the following we simulate the different surveys at the same sky coverage than the W1 field. Doing so, we can directly predict our forecasted gain varying only the number of galaxies in the simulated maps. In summary, the redshift distribution enters our simulations in two ways: first in the number of galaxies generated in the different maps, secondly in the input angular two-point correlation via the Limber's equation (Limber 1954).

³ <http://www.naoj.org/Projects/HSC/>

⁴ <http://sci.esa.int/euclid/>

⁵ <http://www.lsst.org/lsst/>

⁶ <http://www.darkenergysurvey.org/>

⁷ <http://wfirst.gsfc.nasa.gov/>

¹ <http://www.cfht.hawaii.edu/Science/CFHLS/>

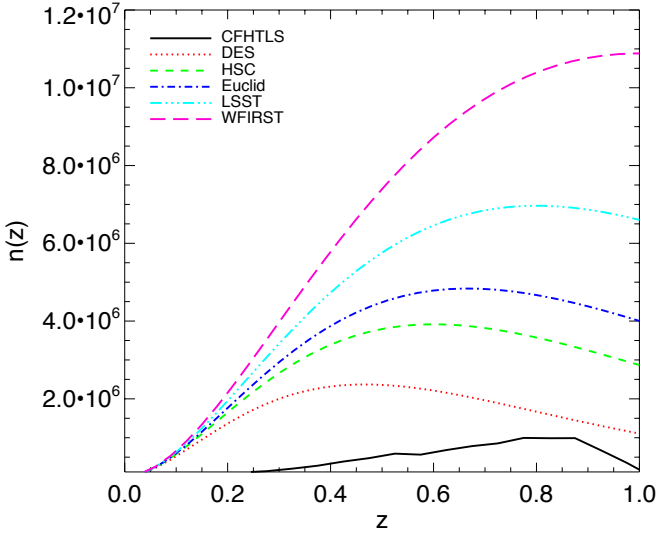
² <http://cosmopmc.info>

Table 2. HOD model parameters obtained by fitting the measured angular two-point correlation function on the CFHTLS data.

Redshift bin	$\log M_{min}$	$\log M_1$	$\log M_0$	$\sigma_{\log M}$	α
$0.2 < z < 0.4$	$12.13^{+0.11}_{-0.16}$	$13.24^{+0.06}_{-0.05}$	$9.67^{+1.15}_{-1.05}$	$0.75^{+0.18}_{-0.29}$	$1.15^{+0.03}_{-0.03}$
$0.4 < z < 0.6$	$12.02^{+0.09}_{-0.17}$	$13.00^{+0.06}_{-0.06}$	$11.93^{+0.15}_{-0.20}$	$0.79^{+0.14}_{-0.36}$	$0.98^{+0.04}_{-0.05}$
$0.6 < z < 0.8$	$12.04^{+0.05}_{-0.06}$	$12.95^{+0.05}_{-0.05}$	$11.80^{+0.15}_{-0.20}$	$0.94^{+0.04}_{-0.04}$	$0.99^{+0.05}_{-0.05}$
$0.8 < z < 1.0$	$12.21^{+0.05}_{-0.05}$	$13.07^{+0.08}_{-0.10}$	$12.42^{+0.14}_{-0.15}$	$0.96^{+0.02}_{-0.07}$	$0.79^{+0.12}_{-0.13}$

Table 4. Specifications of the surveys that enter our prediction pipeline.

Parameter	Description	DES	HSC	Euclid	LSST	WFIRST
z_m	Mean redshift	0.7	0.9	1.0	1.2	1.5
\bar{n}_g	Number density (arcmin^{-2})	10	22	30	50	95

**Figure 1.** Photometric redshift distributions used in the forecasts for the different upcoming surveys. The latter are given by a simple 1-parameter analytic function described in Equation 7. In the case of the CFHTLS-W1 field the redshift distribution is estimated from the data.

3 GENERATION OF MOCK GALAXY AND A^* MAPS AND SPECTRA

To produce simulations of a galaxy count map for a given set of cosmological and HOD parameters, we proceed similarly to Carron et al. (2014). The following summarize the different steps:

(i) The galaxy two-point function $\omega(\theta)$ calculated according to 2.2 is filtered to account for the cell finite size. We then obtain from relation 1 the covariance matrix ω_A of the Gaussian field.

(ii) We generate the Gaussian field and exponentiate it to obtain the galaxy field. Note that the Fourier modes of the Gaussian map are not independent, since the finite volume breaks statistical translation invariance. Standard Fast Fourier Transform (FFT) based methods for Gaussian field generation are thus not applicable for our purposes. We use

the ‘‘circulant embedding’’ method (see Carron et al. 2014, for details).

(iii) We then generate the count map \mathbf{N} from the galaxy field and mask fractions, according to Equation (2), using a standard multinomial sampling algorithm. To take the masks into account, we determine, in a Monte Carlo way, the effective size for each cell which corresponds to the area that is contained in the cell after subtraction of the masks. If the unmasked fraction f of the cell is less than a threshold of 0.3, the cell is considered to contain \bar{N} objects.

(iv) We estimate the angular averaged galaxy power spectrum by discrete Fourier transforming $\delta_{g,i} = N_i/\bar{N}_i - 1$, and averaging over the magnitude of Fourier modes

$$P_g(k) = \frac{1}{V} \frac{1}{N_k} \sum_{q \in \Delta(k)} \left| \tilde{\delta}_g(\mathbf{q}) \right|^2, \quad (8)$$

where N_k is the number of modes in the corresponding bin. In the following, the notation $P(k)$ is used to designate the angular power spectrum with $k = \ell + 1/2$. We use 20 k -bins equally spaced in $\ln k$, k between 240 and 3100. The parameter \bar{N}_i is defined as

$$\bar{N}_i = f_i \left(\frac{N_{\text{tot}}}{\sum_i f_i} \right) \quad (9)$$

We do not subtract any shot noise term, as this does not play a role in the following (see appendix B).

(v) Given a sampling rate \bar{N} , the mapping from N to A^* is defined by the non-linear equation Carron & Szapudi (2014a)

$$A^* + \bar{N} \sigma_A^2 e^{A^*} = \sigma_A^2 \left(N - \frac{1}{2} \right), \quad (10)$$

where $\sigma_A^2 = \ln(1 + \sigma_{\delta_g}^2)$, with $\sigma_{\delta_g}^2$ the variance of the galaxy field fluctuations at the cell scale as predicted by the fiducial model. We transform the count map \mathbf{N} to \mathbf{A}^* solving that equation in each cell with sampling rate \bar{N}_i with an efficient Newton-Raphson algorithm. The mean of the \mathbf{A}^* map and its angular averaged spectrum $P_{A^*}(k)$ is then extracted,

$$P_{A^*}(k) = \frac{1}{V} \frac{1}{N_k} \sum_{q \in \Delta(k)} \left| \tilde{A}^*(\mathbf{q}) \right|^2. \quad (11)$$

Figure 2 shows the comparison between the measurement of the spectra in the CFHTLS data and predictions

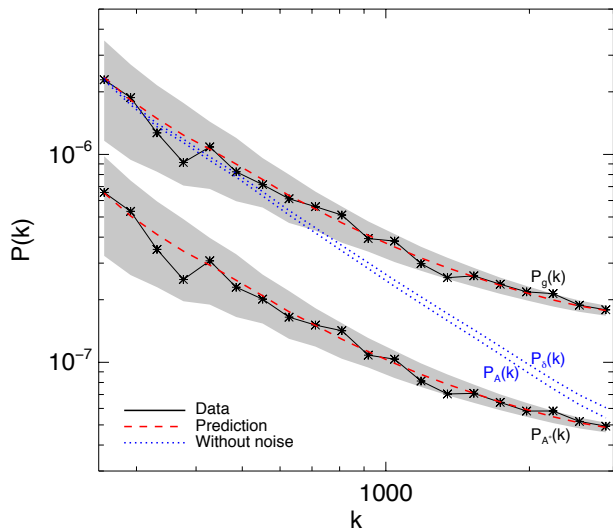


Figure 2. Measurements of both the galaxy angular power spectrum $P_g(k)$ and the non-linear transform A^* power spectrum $P_{A^*}(k)$ on the CFHTLS W1 field in the redshift bin $0.6 < z < 0.8$ (solid black line). The red-dashed lines represent the predictions for both quantities derived as described in Section 2 using $N_{res} = 1000$ realizations. The grey area show the 2σ confidence regions. The blue dotted lines represent the power spectra of the underlying fields δ and $A = \ln(1 + \delta_g)$ and thus illustrate the effect of shot-noise on our predictions.

from the fiducial model obtained (together with their covariance matrices) with the help of a sufficient number of such simulations. Shown are the spectra for the redshift bin $0.6 < z < 0.8$, as well as the 2σ confidence regions (shaded). The dashed line is the prediction from the fiducial model (no fit was performed to these data points, the agreement only reflects that our simulation pipeline reproduces correctly the 2-point statistics of that data set as measured by Wolk et al. 2013). A value of $\chi^2 \sim 0.8$ in both cases indicates that the model captures well the characteristics of both the A^* -power spectrum and the covariance. In addition, the blue dotted lines correspond to the predictions of the power spectra for the underlying fields δ_g and $A = \ln(1 + \delta_g)$.

4 RESULTS

In this Section 4.1, we study the Fisher-matrix forecast gain of using the A^* -power spectrum over of the galaxy power spectrum. We use the following set of cosmological parameters: the energy density of matter Ω_m , the amplitude of the power spectrum of initial conditions quantified in terms of σ_8 , and the dark energy equation of state parameter w_0 . Then in Section 4.2, we compare our predictions to the actual gain measured from the CFHTLS data in the same fashion.

4.1 Fisher forecasts

Given a set of parameters \mathbf{p} , the Fisher matrix provides a means to forecast the results of a likelihood analysis given

model predictions for a data vector \mathcal{O} and sample covariance \mathbf{C} of the observables. The Fisher information matrix for Gaussian data with parameter independent covariance is given by:

$$F_{ij} = \frac{\partial \mathcal{O}^T}{\partial p_i} \mathbf{C}^{-1} \frac{\partial \mathcal{O}}{\partial p_j}. \quad (12)$$

To a first approximation the inverse of the Fisher matrix corresponds to the covariance of the posterior distribution of the parameters one can obtain given the error bars on the data. It means that the larger the value of a Fisher matrix coefficient is, the smaller the variance becomes, and therefore, the tighter the constraints on the unknown parameter value.

In the case of the N -field the observable is the galaxy power spectrum while for the A^* -field the observables are its mean and its spectrum. Our goal in this paper is to quantify the gain using the non-linear transform A^* . We study the information content of our observables by varying one parameter at the time among the set $(\Omega_m, \sigma_8, w_0)$, comparing the values of the matrix (12).

The covariance matrices for all surveys and all redshift bins are estimated according to Section 3 using the two-point correlation function at the fiducial parameters values and $N_{res} = 10,000$ realizations. The derivatives are calculated with finite differences using $N_{res} = 5000$ realizations to estimate the (A^* -) power spectra. Finally, we use Equation 12 to calculate the Fisher matrix. Table 5 shows, as an example, the Fisher matrices derived using on one hand the galaxy power spectrum and on the other A^* for the CFHTLS in the redshift bin $0.6 < z < 0.8$. The use of the non-linear transform A^* provides more information on all the cosmological parameters considered here. However, it is worth noting that w_0 is much less constrained than Ω_m and σ_8 .

Considering Equation 12, one can easily see that the constraining power of a given data point depends on the ratio between the derivative at this data point and its errorbar: the larger the absolute value of the ratio is, the greater the constraining power. Then, a crucial aspect in understanding our forecasts is to analyse how the different cosmological parameters affect the galaxy clustering and then enter our predictions.

The two-point correlation function of the galaxy field at large scales can be written as:

$$\omega \propto [b\sigma_8 D(a)]^2, \quad (13)$$

where D is the growth factor and where the bias b and σ_8 are kept fixed to their fiducial values. Since increasing Ω_m implies more growth, keeping the value of σ_8 fixed at $z = 0$, leads to a decrease of the clustering strength at higher z . For the same reason, increasing σ_8 results in an increase in the clustering strength. Thus the derivatives with respect to Ω_m and σ_8 have opposite signs, and the combination $\Omega_m - \sigma_8$ is tightly constrained, while their sum is not. This can be seen on the upper left panel of the Figure 3 which represents the comparison between the forecast confidence levels on Ω_m and σ_8 obtained using the galaxy power spectrum (solid black line) and A^* (red dashed line). To quantify the improvement using the latter let us consider the 95% confidence contours. The respective areas for the two estimators are 0.027 and 0.017, corresponding to a gain of about 1.26

in the error bars. As example of our gain expectations for an upcoming survey, the lower left panel of Figure 3 illustrates the confidence levels for the WFIRST in the same redshift bin. Unsurprisingly, the constraints on both Ω_m and σ_8 are tighter compared to those from the CFHTLS. The areas of the 95 percent confidence contours are 0.0158 and 0.008 using respectively the power spectrum and A^* , corresponding to a gain of 1.37 in the error bars.

Our main result is presented in Figure 4, showing the predicted improvement in the information on w_0 (left panel) and σ_8 (right panel) for the upcoming surveys as a function of redshift. The quantity plotted is the ratio between the N and A^* Fisher matrix elements, in that sense, it represents the expected information gain using the non-linear transform A^* instead of the power spectrum. The simplest interpretation of this gain is an effective gain in survey area. The gain for Ω_m follows closely the one for σ_8 as the Fisher matrix coefficients are of the same order.

From Figure 4, one can easily see that two different trends emerge: first using A^* is more powerful at low redshifts where the non-linearities are stronger, second this new observable is more efficient for dense surveys such as the WFIRST or the LSST. Table 6 details for each survey the gain (maximum and average) that the new method provides on the different cosmological parameters. In the particular case of the CFHTLS, the gain is only slightly above 1. Moreover, the error bars on the forecast gain for w_0 are large due to the fact that this parameter is not well constrained and thus diminishes the strength of the method. However, even for this less than optimal case, considering the mean value of the gain, A^* performs better than the galaxy power spectrum over the whole redshift range and thus unveils information otherwise hidden. The upper solid lines in both panels show the predictions of the gain without shot-noise. In that regime, A^* reduces to the logarithmic transform of the continuous field and therefore extract all the available information on the cosmological parameters. These lines cannot be crossed and illustrate the upper limit on the information given our chosen configuration.

All the upcoming surveys were designed to be large, they are therefore costly. The use of the optimal observable A^* improves constraints to such a degree that it corresponds to an effective increase of the survey area by up to a factor of 2. Moreover, the largest gains are predicted at low redshift, exactly where the dark energy is constrained the most efficiently. As a result, we expect “sufficient statistics” to be a powerful method to improve the future constraints on the various cosmological parameters, just by using an alternative data analysis strategy.

4.2 Measurements from CFHTLS data

We can go further and compare our predictions to actual measurements on the CFHTLS data. We consider our fiducial model and use the W1 field in the four redshift bins $0.2 < z < 0.4$, $0.4 < z < 0.6$, $0.6 < z < 0.8$ and $0.8 < z < 1.0$ to construct the galaxy counts maps.

Figure 3 shows the results obtained using a joint fit of the cosmological parameters (Ω_m, σ_8) for both the galaxy power spectrum (middle panel) and the A^* -power spectrum (right panel). The measurements are made in the redshift bin $0.6 < z < 0.8$ and our predictions are derived with

Table 5. Fisher matrices for the CFHTLS-W1 field in the redshift bin $0.6 < z < 0.8$. The upper right coefficients and each of the first coefficients on the diagonal are obtained using the galaxy spectrum. The lower left coefficients and the second on the diagonal are obtained using A^* . The diagonal elements are increased using A^* while the off-diagonal elements decrease.

	σ_8	Ω_m	w_0
σ_8	2517/2918	-2234	868
Ω_m	-2518	2189/2614	-794
w_0	1005	-911	303/351

Table 6. Information gain (max/average) for the different cosmological parameters.

	σ_8	Ω_m	w_0
CFHTLS	1.17/ 1.15	1.25/ 1.17	1.17/ 1.16
HSC	1.82/ 1.45	1.70/ 1.37	1.83/ 1.44
Euclid	1.89/ 1.48	1.78/ 1.41	1.86/ 1.46
DES	1.78/ 1.38	1.64/ 1.34	1.76/ 1.36
LSST	1.90/ 1.53	1.83/ 1.44	1.86/ 1.49
WFIRST	1.98/ 1.59	1.87/ 1.48	1.98/ 1.55

$N_{res} = 100$. One can recognize for the two observables the usual “banana” shape for the contours on Ω_m and σ_8 . This shape is roughly reproduced by the dotted line which is given by Equation 13. This shows that the large scale behavior of the two-point correlation function can explain the general trend of our measurements but also that small scale contributions enter our predictions and result in more subtle effects. The contours represent, as before, the 68%, 95% and 99% confidence levels. As a comparison, we perform the same analysis on a simulated map for the WFIRST survey also in the redshift bin $0.6 < z < 0.8$. This is shown on the bottom middle and right panels of Figure 3. We see the “banana” shape for the contours of the galaxy power spectrum and A^* , we also observe that using the latter the contours on Ω_m and σ_8 shrink, leading to better constraints on these two parameters in a way that mirrors well the predictions made before using the Fisher forecast.

We can also compare the expected gains on Figure 4 for the two parameters σ_8 and w_0 to the gain directly measured on the data. We proceed as followed:

(i) For each redshift bin we construct the galaxy counts maps of W1.

(ii) Fixing everything else and varying one cosmological parameter at a time, we fit our predictions for both the galaxy power spectrum and the A^* -power spectrum to the ones measured on the maps. We use a χ^2 -technique on a 200-points grid going from $[-2.0, 0]$ for w_0 and $[0.4, 1]$ for σ_8 respectively with $N_{res} = 200$.

(iii) Our simulations are made with a finite number of realizations which results in noisy posteriors (as it can be seen on the first panel of Figure 5). It is thus not clear how to estimate their variances directly. However, the estimated “chi-squared”, $\chi^2_{N_{res}}$, is a well-behaved function as its errors bars are symmetric around the mean value as shown

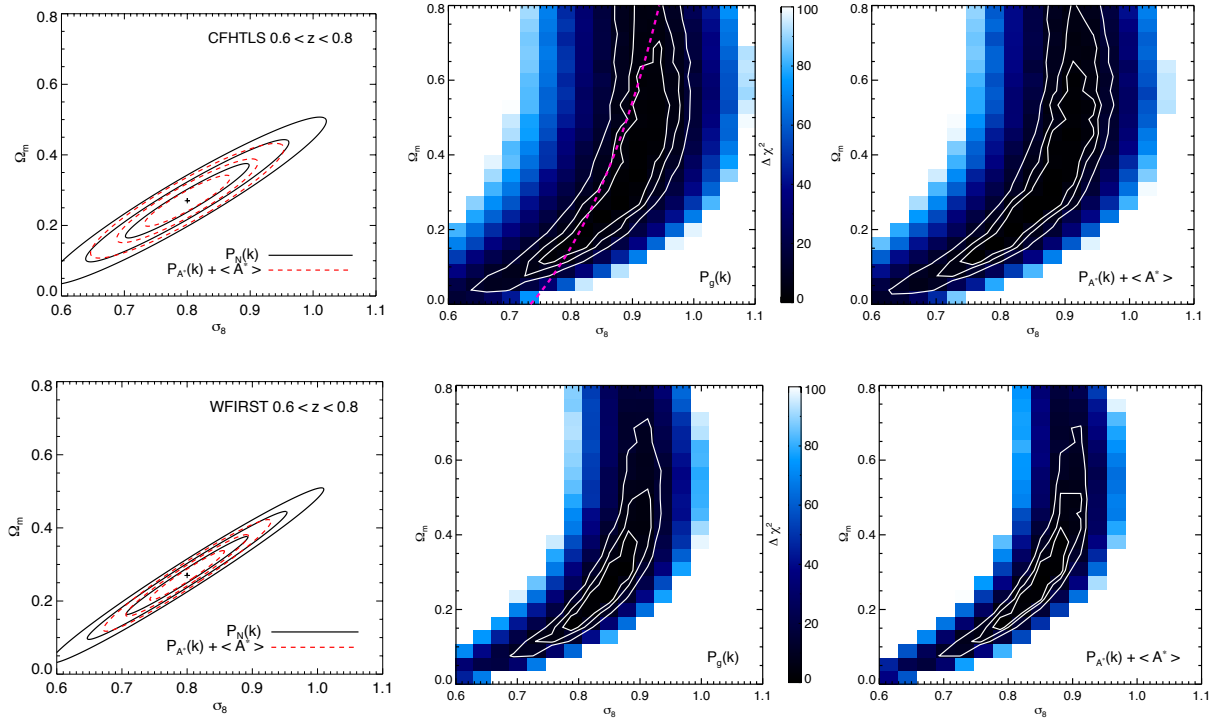


Figure 3. Comparison of the 68%, 95% and 99% confidence levels on Ω_m and σ_8 . We take as illustrative example the bin $0.6 < z < 0.8$, both for the CFHTLS (upper panels) and the WFIRST (bottom panels). The upper and bottom right panels show the contours obtained using the power spectrum (solid black line) and A^* (red dashed line) for both the CFHTLS and the WFIRST with a Fisher matrix analysis. The middle panels show the actual measurements for the confidence levels on the CFHTLS (top) and on a simulated map of the WFIRST (bottom) using the galaxy power spectrum. The dotted line illustrates the relation in Equation 13. The right panels shows the same measurements using instead A^* .

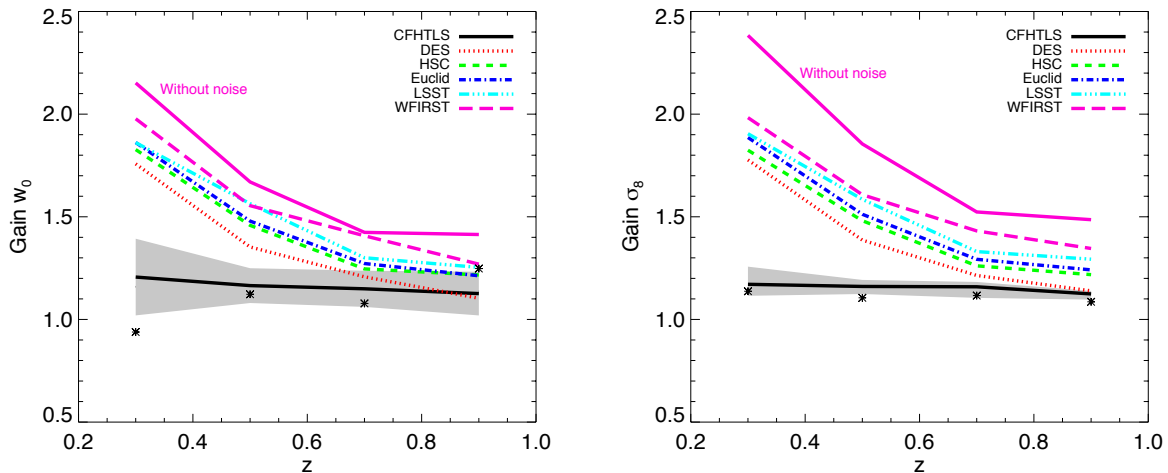


Figure 4. Forecast information gains on the cosmological parameters w_0 (left panel) and σ_8 (right panel) using A^* instead of the galaxy power spectrum for the CFHTLS (solid black line) and a list of future surveys in the redshift range $0.2 < z < 1.0$. The black stars represent the comparison with actual measurements of this gain on the CFHTLS data and the shaded areas show the 1σ confidence limits for the forecasts derived as described in Section 4.2. The errors bars are larger in the case of w_0 as this parameter is less constrained by the data. The upper solid lines, in both panels, show the case with no shot noise and thus represent the limit of the maximum information that one can extract given our ℓ -range.

in Appendix A. We fit to its values a 4-th order polynomial which gives us an analytical expression for $\chi^2_{N_{res}}$ and therefore for a “smoothed” version of the posteriors. If the posteriors were Gaussian, they will be described by a 2-th order polynomial. These steps are summarized in Figure 5.

(iv) We then estimate the variances of the “smoothed” posteriors obtained using both A^* and the galaxy power spectrum and finally take the ratio of the two to measure the gain.

The results are represented by the black stars on Figure 4. We see some discrepancies compared to the forecast value of the gain especially for the less constrained parameter w_0 . To discriminate between a tension or just an effect of the variability in our data, we estimate the uncertainties on the forecast gain by repeating the steps above for 100 simulated data maps of W1. We then use the variance of the obtained ratios as an estimator of the uncertainties on our forecast gains which are illustrated by the 1σ confidence regions (the shaded areas) in Figure 4. We see that within the error bars the overall agreement with the predictions is good meaning that our statistical model captures and reproduces accurately the behavior of the data. All of the above demonstrates that the prediction pipeline implemented in that study describes precisely the statistical properties of the data and therefore shows that our predictions for the upcoming surveys and the expected gain for A^* are both realistic and robust.

5 DISCUSSION AND PROSPECTS

It was known that non-linear transforms help to capture more efficiently the information encoded in the matter density field. In this work, we have shown, in a quantitative way, that there is room for improvement beyond the galaxy power spectrum for the clustering of the large scale structures using a new observable A^* derived to be the “sufficient statistics” in the case of the galaxy field. We have developed a simulations pipeline which include all the main sources of statistical uncertainties (super survey modes, galaxy trispectrum, discreteness effects) and calibrated our modelling on actual data coming from one of the state-of-art large photometric redshift surveys available at the time: the CFHTLS. From this pipeline we were able to simulate, using a large number of realizations, both the galaxy and the A^* power spectra.

We have demonstrated that our statistical modeling is accurate and captures correctly the statistical properties of the measurements. We have compared the efficiency forecast for the galaxy power spectrum and the mean and spectrum of A^* for the CFHTLS to measurements on this data set. In this particular case, the gain using the non-linear transform is modest, especially for parameters that are not well constrained by the data. The promise of the new observable is larger for upcoming surveys. We found that with higher signal to noise, the gain on the information on the three cosmological parameters Ω_m , σ_8 and w_0 is up to about a factor of 2, especially at low redshifts and for dense surveys.

During the practical implementation of this estimator, we needed to solve some technical difficulties that are unique

to this method. First, as we used a finite number of realizations to predict the power spectrum, the obtained posteriors for the different parameters are noisy. We described in Appendix A that our errors on the parameters even if noisy converge very fast needed only a reasonable amount of realizations and we suggested a practical method to obtain smooth posteriors. Second, for the same reasons, this method, as it mirrors the statistical uncertainties of the measurements, works better for parameters that are well constrained; this is a perfect fit for high precision cosmological applications.

Despite that the technology of estimation is admittedly slightly more complex (and we provided a detailed description of complexities and how to mitigate them), we have shown that “sufficient statistics” increase the statistical constraining power of upcoming surveys to the point that the additional effort is worth the consideration. In a future work, we will use this new optimal observable to put simultaneous constraints on both the HOD and the cosmological parameters, testing the effects of priors and of the combination of different independent measurements, e.g., in combination with Planck (Planck Collaboration et al. 2014). Another natural extension of A^* will be to derive the “sufficient statistics” for the galaxy shear field. While this is less straightforward due to the mass-sheet degeneracy (Carron & Szapudi 2014b, e.g.), in combination with additional measurements, such as the galaxy clustering and the galaxy-galaxy lensing, it will provide optimal constraints on cosmological parameters.

6 ACKNOWLEDGMENTS

The authors thank Suhrud More, Masahiro Takada and Alexie Leauthaud for useful conversations.

The authors acknowledge NASA grants NNX12AF83G and NNX10AD53G for support.

Part of this work was based on observations obtained with MegaPrime/MegaCam, a joint project of CFHT and CEA/IRFU, at the Canada-France-Hawaii Telescope (CFHT) which is operated by the National Research Council (NRC) of Canada, the Institut National des Science de l’Univers of the Centre National de la Recherche Scientifique (CNRS) of France, and the University of Hawaii. This work is based in part on data products produced at Terapix available at the Canadian Astronomy Data Centre as part of the Canada-France-Hawaii Telescope Legacy Survey, a collaborative project of NRC and CNRS.

APPENDIX A: ESTIMATION OF THE LIKELIHOOD WITH A FINITE NUMBER OF SIMULATIONS

We use a finite number of simulations to obtain the model predictions at each point in parameter space. We discuss in this section how this impacts the calculation of the parameter posteriors, allowing the assessment of the ‘errors on the parameters errors’. We find that this effect broadens only slightly the width of the parameter posterior according to Equation (A7).

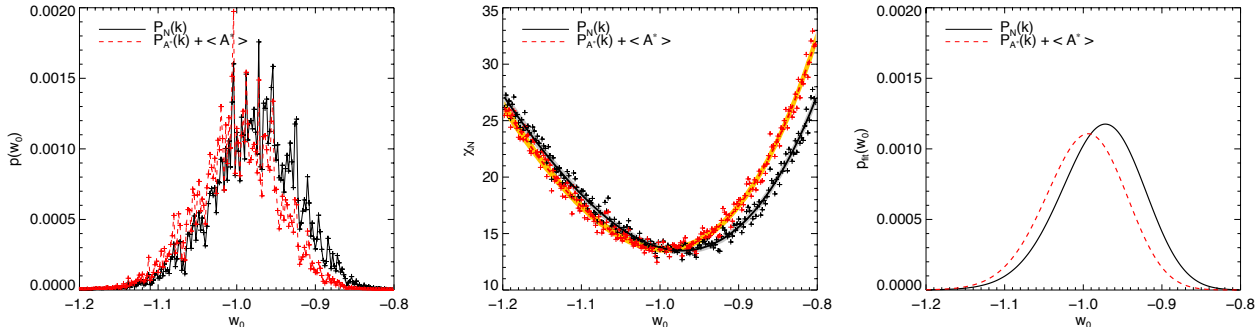


Figure 5. An example to illustrate the procedure to estimate the variance of the posteriors. Here we fit the cosmological parameter w_0 on the CFHTLS data in the redshift bin $0.6 < z < 0.8$. The left panel show the noisy posteriors obtained using the galaxy power spectrum (solid black line) and A^* (red dashed line). To have an estimate of the variances of these posteriors, we fit χ^2_N with a 4-th order polynomial using the error bars described in Appendix B. The middle panel illustrates this procedure and show the best fit overplotted to the measurements (red and black symbols). The right panel shows the “smoothed” posterior estimated from the best fit values for both the galaxy power spectrum (solid black line) and A^* (red dashed line).

The likelihood for the model parameters is proportional to $e^{-\chi^2/2}$, where

$$\chi^2(\boldsymbol{\theta}) = (\mathbf{d} - \bar{\mathbf{d}}(\boldsymbol{\theta})) \cdot \Sigma^{-1} (\mathbf{d} - \bar{\mathbf{d}}(\boldsymbol{\theta})), \quad (\text{A1})$$

where \mathbf{d} is the data vector (in our case the spectra and/or mean of \mathbf{A}^*) and $\bar{\mathbf{d}}$ the predictions. In this paper, we evaluate the predictions at each point in parameter space by averaging over N_{res} simulations of the data. Therefore, the true χ^2 is estimated with some error and bias by

$$\hat{\chi}_{N_{res}}^2(\boldsymbol{\theta}) = (\mathbf{d} - \hat{\mathbf{d}}_{N_{res}}(\boldsymbol{\theta})) \cdot \Sigma^{-1} (\mathbf{d} - \hat{\mathbf{d}}_{N_{res}}(\boldsymbol{\theta})), \quad (\text{A2})$$

where $\hat{\mathbf{d}}_{N_{res}}$ is the average over N_{res} simulations of the data vector. Since the simulations are independent, the central limit theorem implies that for reasonably large N_{res} the estimate $\hat{\mathbf{d}}_{N_{res}}$ will be a Gaussian vector, even if \mathbf{d} is not. The mean of $\hat{\mathbf{d}}_{N_{res}}$ is $\bar{\mathbf{d}}$ and its covariance matrix Σ/N_{res} . The PDF for $\hat{\chi}_{N_{res}}^2$ can be given in closed form (it is basically a non-central χ^2 variable). Again, it will be for all practical purposes a Gaussian. Its bias with respect to the true χ^2 and its variance can be straightforwardly calculated from the above expression, with the result

$$\langle \hat{\chi}_{N_{res}}^2 \rangle - \chi^2 = \frac{N_d}{N_{res}}, \quad \text{Var}(\hat{\chi}_{N_{res}}^2) = \frac{2N_d^2}{N_{res}^2} + \frac{4}{N_{res}} \chi^2, \quad (\text{A3})$$

where N_d is the dimension of the data vector. Thus, the estimated (unnormalized) parameter likelihood

$$\hat{p}_{N_{res}} \propto \exp(-\hat{\chi}_{N_{res}}^2(\boldsymbol{\theta})/2) \quad (\text{A4})$$

is the exponential of a Gaussian variable, i.e. a lognormal variable at each point in parameter space. Furthermore, the estimates at different points are independent. With this at hand, we can then ask how well we can measure some properties of the parameter posterior. Assuming the prior does not play a role, estimates of some function $f(\boldsymbol{\theta})$ such as the mean or variance of the posterior read on average

$$\left\langle \frac{\int d\boldsymbol{\theta} f(\boldsymbol{\theta}) \hat{p}_{N_{res}}(\boldsymbol{\theta})}{\int d\boldsymbol{\theta} \hat{p}_{N_{res}}(\boldsymbol{\theta})} \right\rangle = \frac{\int d\boldsymbol{\theta} f(\boldsymbol{\theta}) \langle \hat{p}_{N_{res}}(\boldsymbol{\theta}) \rangle}{\int d\boldsymbol{\theta} \langle \hat{p}_{N_{res}}(\boldsymbol{\theta}) \rangle}. \quad (\text{A5})$$

Fluctuations from that relation decaying away with the number of points with which the likelihood is sampled. With

Equation (A4), Equation (A3) and the fact that $\langle e^x \rangle = e^{\langle x \rangle + \text{Var}(x)/2}$ for Gaussian x , the expectation value of $\hat{p}_{N_{res}}$ can be calculated with uncomplicated algebra. The result is very simply

$$\langle \hat{p}_{N_{res}}(\boldsymbol{\theta}) \rangle \propto \exp\left(-\frac{1}{2}\chi^2(\boldsymbol{\theta})\left(1 - \frac{1}{N_{res}}\right)\right). \quad (\text{A6})$$

The correction is due to the second term in the variance in Equation (A3), the first term and the bias in that equation being absorbed in the normalization constant. We can conclude that the posterior is only slightly homogeneously broadened. In particular, if the true posterior is roughly Gaussian, the inference parameter (co)variance is slightly larger,

$$\frac{\sigma_{\boldsymbol{\theta}}^{\text{inferred}}}{\sigma_{\boldsymbol{\theta}}^{\text{true}}} = \sqrt{\frac{N_{res}}{N_{res} - 1}}. \quad (\text{A7})$$

These results are illustrated in Figure A1.

APPENDIX B: MULTINOMIAL VERSUS POISSON SAMPLING

Two natural choices of discrete sampling of the underlying field to represent the projected counts are Poisson sampling, where the number of galaxies in each cell field is drawn from a Poisson distribution, and multinomial statistics, where a fixed number of galaxies in distributed throughout the map. In this paper we chose the second option, mainly for its simplicity. We describe here some of the differences between the two choices, and show that choosing multinomial or Poisson will not change our results.

There are several conceptual differences between Poisson and multinomial sampling. Two reasons make the latter simpler for our purposes. First, Poisson sampling requires the introduction of an intensity parameter \bar{N} on which the statistics of the map depend. A careful analysis requires then marginalization of this parameter. Second, the number of galaxies on each simulated map is the same for multinomial sampling. As a consequence the shot-noise term in the galaxy power spectrum is a constant. We do not need to

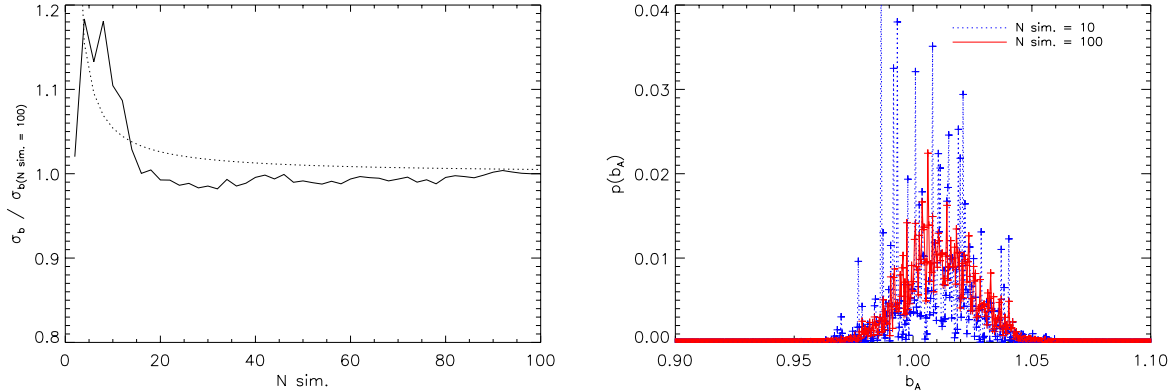


Figure A1. A test case showing the evaluation of the parameter posterior (here for a bias parameter in the log-density) from the extraction of the spectrum $P_g(k)$, as a function of the number of simulations at each point in parameter space used to obtain the model predictions for the spectrum. The lower panel shows the posterior for $N = 10$ and 100 simulations. The upper panel shows as a function of N the square root of the variance of the posterior, normalized to its value found for $N = 100$. Since the wild fluctuations in the posterior are uncorrelated, the variance (or other averages) takes a well-defined value even for moderate N . The dashed line on the upper panel is $\sqrt{N/(N-1)}$, Equation (A7), predicted by the simple arguments in this section.

consider it or subtract it in our analysis, as constant does not affect the information content of a statistic.

Naively one might be worried that the absence of fluctuations in the number of galaxies for multinomial sampling underestimates the total variance of the count maps. However, we found that this lower stochasticity precisely corresponds to the careful treatment of the shot noise term in the case of Poisson sampling. In more details, we found that the following approach is equivalent to the multinomial sampling adopted in the text :

(i) After generation of the lognormal field, we use Poisson sampling to obtain the count map. To this effect, the intensity parameter of the poisson sampling in cell i is taken to be

$$\bar{N}_i = f_i \rho_{g,i} \bar{N} \quad (\text{B1})$$

where \bar{N} is a free parameter, interpreted as the ensemble average number of galaxies in a totally unmasked cell. In the case of the CFHTLS data, we estimated it through

$$\bar{N} = \frac{N_{\text{tot}}}{\sum_i f_i} \quad (\text{B2})$$

(ii) In the galaxy power spectrum we then subtract the shot-noise term. This requires first for each simulated map an estimate \hat{N} of \bar{N} . We use for this the above equation (B2), where N_{tot} now varies from map to map. Defining then $\delta_{g,i} = N/(f_i \hat{N}) - 1$ we can calculate the shot-noise contribution, that we then subtract to the spectrum. It is given by

$$P_g^{\text{shot}}(k) = \frac{V}{d\hat{N}} \left(\frac{1}{d} \sum_{f_i \neq 0} \frac{1}{f_i} \right) \cdot \frac{1}{\hat{n}} \left(\frac{1}{d} \sum_i f_i \right) \left(\frac{1}{d} \sum_{f_i \neq 0} \frac{1}{f_i} \right) \quad (\text{B3})$$

On the right hand side \hat{n} is the observed density of galaxies N_{tot}/V , and d the number of cells. Note that there is no need to subtract a shot-noise term in the A^* power spectrum even for Poisson sampling, as the non-linear transformation already takes into the noise properties of the data.

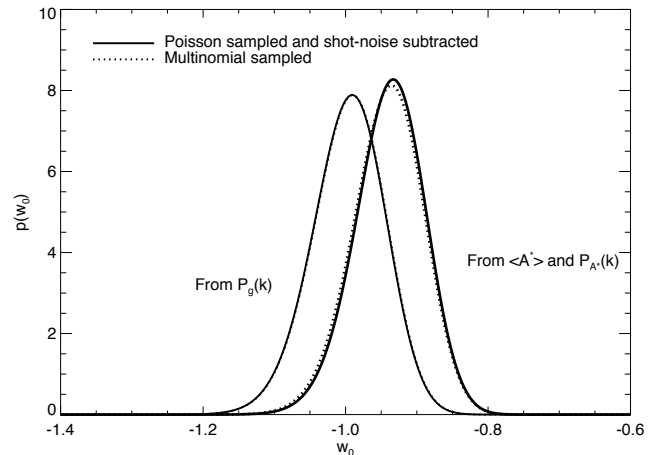


Figure B1. An illustration of the equivalence of multinomial (used in the paper) and Poisson sampling for our purposes. The figure shows the posterior of the dark energy equation of state w_0 obtained by fitting the spectrum of the dark energy of state w_0 or the mean and spectrum of A^* . The dotted line shows the constraints using Poisson sampling, which requires the introduction of a sampling intensity parameter, its estimation from each simulated map and subtraction of the estimated shot noise component. Multinomial sampling shown as the solid lines lead to the same results with no need for any of these steps.

Figure B1 illustrates that the two procedures leads to almost identical results. Shown is the posterior for w_0 using δ_g or A^* using the redshift bin $0.6 < z < 0.8$ of the W1 field of CFHTLS data, using Poisson sampling (dotted) as described above and using multinomial sampling (solid) as described in the main text. The curves are virtually indistinguishable.

REFERENCES

- Carron J., Szapudi I., 2013, MNRAS, 434, 2961
Carron J., Szapudi I., 2014a, MNRAS, 439, L11
Carron J., Szapudi I., 2014b, ArXiv e-prints
Carron J., Wolk M., Szapudi I., 2014, MNRAS, 444, 994
Cole S. et al., 2005, MNRAS, 362, 505
Cooray A., Sheth R., 2002, Phys. Rep., 372, 1
Coupon J. et al., 2012, A&A, 542, A5
de Putter R., Wagner C., Mena O., Verde L., Percival W. J., 2012, J. Cosmology Astropart. Phys., 4, 19
Joachimi B., Taylor A. N., 2011, MNRAS, 416, 1010
Kravtsov A. V., Berlind A. A., Wechsler R. H., Klypin A. A., Gottlöber S., Allgood B., Primack J. R., 2004, ApJ, 609, 35
Li Y., Hu W., Takada M., 2014, Phys. Rev. D, 89, 083519
Limber D. N., 1954, ApJ, 119, 655
Ma C.-P., Fry J. N., 2000, ApJ, 543, 503
Navarro J. F., Frenk C. S., White S. D. M., 1997, ApJ, 490, 493
Neyrinck M. C., Szapudi I., 2007, MNRAS, 375, L51
Neyrinck M. C., Szapudi I., Rimes C. D., 2006, MNRAS, 370, L66
Neyrinck M. C., Szapudi I., Szalay A. S., 2009, ApJ, 698, L90
Peacock J. A., Smith R. E., 2000, MNRAS, 318, 1144
Peebles P. J. E., 1980, The large-scale structure of the universe
Planck Collaboration et al., 2014, A&A, 571, A16
Rimes C. D., Hamilton A. J. S., 2005, MNRAS, 360, L82
Rimes C. D., Hamilton A. J. S., 2006, MNRAS, 371, 1205
Soccimarro R., Sheth R. K., Hui L., Jain B., 2001, ApJ, 546, 20
Seljak U., 2000, MNRAS, 318, 203
Seo H.-J., Sato M., Dodelson S., Jain B., Takada M., 2011, ApJ, 729, L11
Sheth R. K., Tormen G., 1999, MNRAS, 308, 119
Szapudi I., 2009, in Martínez V. J., Saar E., Martínez-González E., Pons-Bordería M.-J., eds, Lecture Notes in Physics, Berlin Springer Verlag Vol. 665, Data Analysis in Cosmology. pp 457–492
Szapudi I., Colombi S., 1996, ApJ, 470, 131
Takada M., Hu W., 2013, Phys. Rev. D, 87, 123504
Takada M., Jain B., 2009, MNRAS, 395, 2065
Tegmark M. et al., 2004, Phys. Rev. D, 69, 103501
Tinker J. L., Weinberg D. H., Zheng Z., Zehavi I., 2005, ApJ, 631, 41
Wolk M., McCracken H. J., Colombi S., Fry J. N., Kilbinger M., Hudelot P., Mellier Y., Ilbert O., 2013, MNRAS, 435, 2
Zheng Z. et al., 2005, ApJ, 633, 791
Zheng Z., Coil A. L., Zehavi I., 2007, ApJ, 667, 760